Next Materials 7 (2025) 100370

Contents lists available at ScienceDirect

Next Materials

journal homepage: www.sciencedirect.com/journal/next-materials

Research article

Synergistic effects in magnetically recoverable nanocomposites of CuO nanoleaves with Fe_3O_4 nanoparticles for organic dye degradation

César Leandro Londoño-Calderón [a], Pablo Tancredi [b,c,*], Sandra Menchaca-Nal [d,e], Nora J. Francois [d,e], Laura G. Pampillo [c,f]

[a] Grupo de Investigación en Física y Matemáticas con Énfasis en la Formación de Ingenieros, Departamento de Física y Matemáticas, Facultad de Ingeniería, Universidad Autónoma de Manizales, Antigua Estación del Ferrocarril, Manizales CP 170001, Colombia
[b] Functional Nanomaterials, INTI-Micro and Nanotechnology, National Institute of Industrial Technology (INTI), Av. Gral. Paz No 5445, San Martín, Buenos Aires, Argentina
[c] CONICET, Universidad de Buenos Aires, Instituto de Tecnologías y Ciencias de la Ingeniería "Hilario Fernández Long" (INTECIN), Av. Paseo Colón 850, Buenos Aires C1063ACV, Argentina
[d] Universidad de Buenos Aires, Facultad de Ingeniería, Grupo de Aplicaciones de Materiales Biocompatibles (GAMBI), Departamento de Química, Av. Paseo Colón 850, Buenos Aires C1063ACV, Argentina
[e] CONICET, Universidad de Buenos Aires, Instituto de Tecnología en Polímeros y Nanotecnología (ITPN), Av. Las Heras 2214 (1127), Buenos Aires, Argentina
[f] Universidad de Buenos Aires, Facultad de Ingeniería, Laboratorio de Sólidos Amorfos, Av. Paseo Colón 850, Buenos Aires C1063ACV, Argentina

ARTICLE INFO

Keywords:
Magnetic nanoparticles
Nanoleaves
Cupric oxide
Magnetite
Nanocomposites
Catalytic degradation
Water remediation
Methyl orange

ABSTRACT

In this work, we report the synthesis and characterization of Fe_3O_4/CuO nanocomposites and demonstrate their catalytic efficiency towards the degradation of organic dyes. Single-crystalline Fe_3O_4 nanoparticles of 11 nm were obtained via coprecipitation and functionalized with β-alanine for colloidal stability and chemical affinity towards the CuO surface. The CuO nanoleaves were produced by sonochemical precipitation, resulting in nanostructures with average sizes of 1080, 286, and 15 nm in long, wide, and thick, respectively. Moreover, the nanoleaves are polycrystalline, with an average crystallite size of 16 nm, and with band-gap energy of 1.48 eV. The nanocomposites were prepared by mixing the two nanostructures in various ratios to study the effect of the composition on both properties and technological performance. Field emission scanning electron microscopy confirmed that the ratio of primary nanostructures was retained in the nanocomposites and showed that the exposed surface area of nanoleaves decreased with an increasing percentage of Fe_3O_4 nanoparticles. While the crystalline structure of the primary nanostructures remained unchanged, the band-gap energy increased to 1.78 eV. These nanocomposites demonstrated impressive catalytic efficiency, achieving nearly complete degradation of methyl orange with H_2O_2 assisted by ultrasonication. This high catalytic activity, coupled with ease of recovery and reuse, makes these nanocomposites a promising solution for water remediation applications.

1. Introduction

The persistent concern about water pollution with various contaminants has prompted intensified efforts to develop diverse strategies to effectively clean wastewater and improve water sources [1,2]. Many industries, such as textile, pharmaceutical, and food, apply different types of dyes in manufacturing their products, which causes severe problems in the watercourses where they are dumped. The presence of dyes in effluents, even in minimal quantities, diminishes sunlight penetration through water, reducing the photosynthesis mechanism of aquatic plants. Moreover, these dyes are toxic to living organisms, including humans [3]. These harmful organic contaminants are difficult to treat due to their complex and stable structures [4]. Among others, methyl orange (MO) is a water-soluble synthetic dye that is harmful to the environment and life and is often used as a model anionic compound in water remediation research [5].

Various chemical, biological, and physical methods have been used to remove dyes from wastewater streams and natural water, like chemical oxidation [6], membrane separation [7], bio decolorization [8], coagulation/flocculation [9,10], and adsorption [11]. Although all

* Corresponding author at: Functional Nanomaterials, INTI-Micro and Nanotechnology, National Institute of Industrial Technology (INTI), Av. Gral. Paz No 5445, San Martín, Buenos Aires, Argentina
E-mail address: ptancredi@fi.uba.ar (P. Tancredi).

https://doi.org/10.1016/j.nxmate.2024.100370
Received 30 April 2024; Received in revised form 2 September 2024; Accepted 4 September 2024
Available online 13 September 2024

these methods are efficient in removing contaminants, they also can present some disadvantages, such as high costs and processes that do not respect the environment. In this context, advanced oxidation processes (AOPs) [12,13] have arisen as one of the most promising alternatives, and catalysts based on inorganic semiconductor nanomaterials have properties that make them especially interesting for these applications. In this scenario, in our previous work [14], we demonstrated the high efficiency of cupric oxide nanoleaves (from here on, CuO NLs) toward the catalytic oxidative degradation of MO dye and its feasible recovery by centrifugation (2000 rpm). However, catalyst isolation by centrifugation, as well as liquid-liquid extraction, chromatography, or filtration involves time-consuming and tedious protocols [15,16]. This is why magnetic separation has emerged as a robust and highly efficient process, and the field of recyclable magnetic nanocatalysts has drawn considerable research interest due to its importance in practical applications [17–20]. Early strategies focused on using magnetic nanoparticles as an alternative to conventional inert supports (polymers, carbon, and metal oxides) to facilitate the separation and recovery of catalysts with simple magnets. In this way, the nanoparticles could support other catalytic nanomaterials and be the active magnetic component for magnetic recovery [21].

Among all magnetic nanoparticles, magnetite is the most-exploited iron oxide nanomaterial for magnetic separation procedures [18]. Magnetite is a black, ferrimagnetic at room temperature, and almost metallic mineral with a high Curie temperature and a relatively high saturation magnetization [22]. Magnetite nanoparticles (from here on, Fe_3O_4 NPs) have already been employed for the catalytic degradation of dyes like methyl orange (MO) [23,24]. However, most reported cases using this material solely require high temperatures, complex reactors, or microwave irradiation, among other complications. To solve these problems, composites made of magnetic materials with active catalysts have been proposed as alternatives to overcome these difficulties. But, the high cost of some precursors, the complicated fabrication processes, the long degradation times ($>$ 1 h), and the high catalyst dosage required are still unsolved issues among these materials. In this context, Fe_3O_4 and CuO nanocomposites appear promising for some environmental applications, with an emerging but interesting background in specialized literature. For instance, few reports are showing that composites containing CuO@Fe_3O_4 can be effective materials for the degradation and removal of organic dyes, either as the unique components of the composite [25] or as a part of more complex systems with ZnO [26,27], TiO_2 [28], or carbon-based materials [29,30].

Despite the great efforts made so far, the development of economical, simpler, and environmentally friendly magnetic nanocatalysts that can be easily recovered using an external magnet without significant loss of catalyst material or catalytic activity remains an open challenge. Therefore, this work aimed to fabricate a set of magnetically recoverable nanocomposites of CuO NLs with functionalized Fe_3O_4 NPs by a non-demanding synthesis strategy, to exploit the synergistic effect of both materials as a low-cost and easily recoverable magnetic nanocatalysts towards the degradation of organic contaminants. Throughout the work, we studied the morphology, chemical composition, crystalline structure, and optical properties of three nanocomposites with varying proportions of CuO NLs and Fe_3O_4 NPs. After this analysis, we also studied the performance of each sample towards the degradation of organic contaminants, linking these results to the structural properties presented before.

2. Experimental section

2.1. Chemicals

Copper (II) chloride dihydrate ($CuCl_2{\cdot}2\ H_2O$), sodium hydroxide (NaOH), chlorohydric acid (HCl, 36 % wt/wt), and ethanol were purchased from Laboratorios Cicarelli. Iron (II) chloride tetrahydrate ($FeCl_2{\cdot}4\ H_2O$) was purchased from Sigma-Aldrich. Iron (III) chloride hexahydrate ($FeCl_3{\cdot}6\ H_2O$), β-Alanine ($C_3H_7NO_2$), ammonium hydroxide (NH_4OH, 25 % wt/wt), and hydrogen peroxide solution (H_2O_2, 30 % wt/wt) were purchased from Anedra Research AG. Methyl orange was purchased from The British Drug House LTD. Distilled water was used for all the experiments. All reagents were of analytical grade and used as received without further purification.

2.2. Synthesis of Fe_3O_4 NPs functionalized with β-alanine

The Fe_3O_4 NPs were produced by a previously reported method [31]. 8.6×10^{-3} mol of $FeCl_3{\cdot}6\ H_2O$ and 4.3×10^{-3} mol of $FeCl_2{\cdot}4\ H_2O$ were added to a beaker containing 100 mL of deoxygenated water. The salts were dissolved under magnetic stirring and co-precipitated with 10 mL of NH_4OH. After 15 minutes, the NPs were magnetically isolated and washed with distilled water several times. Then, the NPs were re-dispersed in 100 mL of a solution containing 1 g of β-alanine and HCl to adjust the pH to 5.5. The dispersion was sonicated for 5 min and then stirred at 90 °C for 2 h. The Fe_3O_4 NPs were centrifuged after precipitation with ethanol 96 % and re-dispersed in water to form a stable ferrofluid.

2.3. Synthesis of CuO NLs

The preparation of the CuO NLs precursor was done following a methodology similar to the one described in our previous report [14], with some minor differences. The precipitation reaction was carried out in an ultrasonic bath at 40 kHz - 55 W by adding in one step a NaOH solution to a beaker with the Cu (II) solution. After 4 h, the black precipitate was filtered and washed with an excess of distilled water and dried until constant weight, with a reaction yield of 99 %.

2.4. Synthesis of CuO NLs with Fe_3O_4 NPs nanocomposites

The CuO NLs with Fe_3O_4 NPs nanocomposites (Fe_3O_4/CuO NCs) were obtained by mixing the two primary nanostructures, i.e., the ferrofluid and a dispersion of the NLs. A series of different nanocomposites were produced by changing the volume of ferrofluid while keeping the NLs concentration constant. First, an aqueous dispersion of CuO NLs (83.5 mL, 0.6 mg/mL) was prepared and sonicated for 15 min. Then, a certain volume of the ferrofluid of concentration 10 mg/mL was mixed with the NLs dispersion under magnetic stirring for 30 min and heated to 65 °C. The black precipitate obtained was magnetically sedimented and dried until constant weight. The volume of ferrofluid was changed between 2,5 mL, 5 mL, and 10 mL to produce the nanocomposites with a Fe_3O_4 NPs fraction of 33 %, 50 %, and 67 %, respectively. The yield of the reactions oscillated between 93 % and 98 %. The samples were named according to the NPs fraction percentage used in the synthesis. A schematic representation of the synthesis process is presented in Scheme 1.

2.5. Characterization methods

The morphology and elemental composition of CuO NLs, Fe_3O_4 NPs, and Fe_3O_4/CuO NCs were studied with a field emission scanning electron microscope (FE-SEM, Zeiss Supra 40), with a field emission gun operating at 3 kV and equipped with an EDX detector. Powder samples were dispersed in distilled water, dropped, and collected in a commercial electrochemical polished aluminum [32]. A free version of the software ImageJ 1.51k was used to analyze the images and to build the histograms of NPs and NLs sizes. A Nano ZS Malvern, model ZEN 3600 was used to determine the hydrodynamic size and the zeta potential of NPs and NLs. NaOH and HCl were used to adjust the solution pH, and the ionic strength was set to 5 mM. The final concentration of NPs or NLs for the measurements was 50 μg/mL. A Thermo Scientific infrared spectrometer, model Nicolet 6700 equipped with an attenuated total reflectance (ATR) cell, was used to acquire the FT-IR spectrum of the

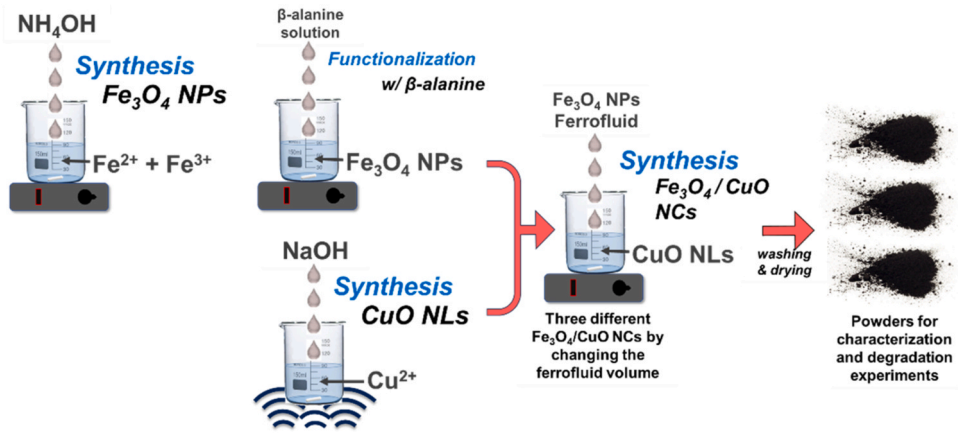

Scheme 1. : Schematic representation of the synthesis process of Fe_3O_4/CuO NCs.

NPs. The spectrum was registered in absorbance mode in the 400 cm^{-1} – 4000 cm^{-1} range. A TGA-50 Shimadzu instrument was used to perform the thermogravimetric analysis (TGA) of the NPs. The temperature program was run from 25 °C to 600 °C at a heating rate of 10 °C/min, under N_2 atmosphere (30 mL/min). The crystallographic structure of NPs, NLs, and Fe_3O_4/CuO NCs was studied by X-ray diffraction. A SmartLab - Rigaku equipment was used with Cu Kα radiation in a range (2θ) from 30° to 90° in Bragg-Brentano mode and a scanning step of 0.02° at 0.5°/min. Optical properties of the NPs, NLs, and Fe_3O_4/CuO NCs were studied by UV-Vis diffuse reflectance measurements using a Shimadzu UV-2401 PC spectrophotometer in the wavelength range of 200 nm - 800 nm. Barium sulfate was used as a reference to provide a nominal 100 % reflectance measurement. The samples were measured as liquid dispersions after sonication for several minutes until uniform coloration was achieved.

2.6. Sonocatalytic degradation of methyl orange

The reaction systems for the degradation experiment were prepared with 10 mL of MO (6 μg/mL), 7 mL of the Fe_3O_4/CuO NCs (74.5 μg/mL), and 1 mL of H_2O_2 (30 % wt/wt). Subsequently, the mixture was sonicated for 1 h at (44 ± 2) kHz - 55 W at dark conditions and the catalyst was recovered using a neodymium magnet afterward. The influence and activity of each experimental variable using bare NLs were already informed in our previous work [14]. The dye degradation efficiency was monitored by means of UV-Vis spectrophotometry. The degradation tests were performed in triplicate, and the results are presented as the mean value with the standard deviation (± SD).

2.7. Recyclability of the Fe_3O_4/CuO NCs

After the methyl orange degradation reaction, the Fe_3O_4/CuO NCs catalysts were recovered with a magnet and re-dispersed in distilled water. This process was repeated three times before using the catalyst in the next degradation experiment. The degradation and recovering experiments were repeated three consecutive times (cycles) to evaluate the recyclability and catalytic efficiency of the Fe_3O_4/CuO NCs. These tests were also performed in triplicate and the results are presented as the mean value with the standard deviation (± SD).

3. Results and discussion

An important step in the design of supported catalysts based on iron oxide is the functionalization of the NPs surface. Among several alternatives, in this work, β-alanine was chosen to link Fe_3O_4 NPs and CuO NLs because of their appropriate affinity (functional groups) and interfacing potential. β-alanine is an amino acid with a carboxylic acid (-COOH) group and a basic primary amine (-NH_2) at the β-position. Carboxylates are known to establish strong coordination bonds with iron oxide surfaces, so the β-alanine is expected to bond to the NPs through this group [31]. The coupling through the β-alanine carboxylate group can lead to a functionalized surface, with the amino-terminal group facing out of the NPs. Amino acids are also known for their high affinity towards copper, with generally very high stability constants [33]. These reasons make β-alanine a good candidate to link Fe_3O_4 NPs and CuO NLs in the synthesis of magnetically retriable catalytic systems.

3.1. Characterization of Fe_3O_4 NPs

Fig. 1(a) shows a TEM image of the functionalized Fe_3O_4 NPs, where it can be observed the presence of nanosized particles with roughly spherical shape. The hydrodynamic diameter was measured at pH = 5 to estimate the size of these aggregates of NPs in the suspension. Fig. 1(b) shows the size histogram of the NPs obtained from more than 600 measurements from different TEM images. The size of the NPs ranges between 5 nm - 25 nm with an average size of (11 ± 5) nm. Fig. 1(c) shows the hydrodynamic diameter distribution, with a mean value of about 61 nm. This size is significantly larger than the diameter of the individual NPs observed in the TEM image. Similar results have previously been reported for Fe_3O_4 NPs coated with polymers of low molecular weight [34]. The difference observed between hydrodynamic and particle diameters suggests that the NPs are forming small agglomerates while suspended in water. However, the size of these agglomerates is small enough to avoid sedimentation for extended times. Fig. 1(d) shows the FT-IR spectrum of the NPs. The broadband centered around 3400 cm^{-1} corresponds to the hydroxyl stretching signal. The asymmetric stretching vibrations of CH_2 at 2922 cm^{-1}, the symmetric stretching of CH_2 at 2854 cm^{-1}, the bending vibration of NH_2 at 1622 cm^{-1}, and the bending vibrations of CH_2 at 1458 cm^{-1} and 1428 cm^{-1} confirm the obtained for the NPs. Fig. 1(e) shows the TGA curve obtained for the NPs. The first weight loss (≈ 4 %) from room temperature to 200 °C is associated with the removal of the remaining moisture in the composite. The second weight loss (≈ 4 %) between 200 and 600 °C is mainly associated with β-alanine decomposition. The TGA of non-functionalized Fe_3O_4 only shows a significant weight loss below 200 °C and remains constant for temperatures above this value due to the absence of organic moieties [35].

The electrokinetic or zeta potential was used to evaluate the stability of the Fe_3O_4 NPs dispersed in water. High values (both positive and negative) of zeta potential indicate good colloidal stability due to the existence of strong electrostatic repulsion forces among the NPs, while values closer to zero suggest that particles have a strong tendency to agglomerate [36]. The measured zeta potential value was (35 ± 4) mV at pH = 5.5, which is slightly higher than the value corresponding to

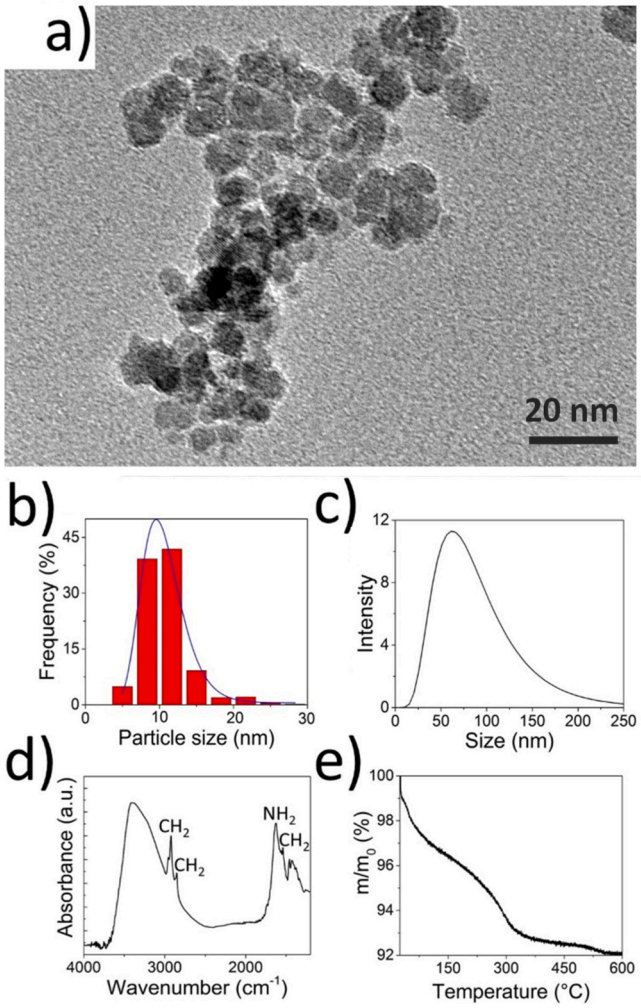

Fig. 1. **(a)** TEM image of Fe_3O_4 NPs. **(b)** Particle size distribution histogram of the NPs. **(c)** Hydrodynamic size distribution of the NPs in aqueous dispersion measured by DLS. **(d)** FTIR spectrum of the NPs. **(e)** TGA curve of NPs.

bare magnetite and confirms the good colloidal stability of the NPs at this pH. At pH 7.0, the zeta potential was (6 ± 3) mV. As expected, zeta potential values of the NPs increase as pH becomes more acidic, and the isoelectric point is estimated to be barely above pH = 7.0, a slightly higher value than previously reported of bare magnetite [37]. These results suggest that the protonation/deprotonation behavior of the NPs is governed by both the exposed iron oxide surface and the β-alanine molecules.

3.2. Characterization of CuO NLs

Fig. 2(a) shows the morphological details of the CuO NLs obtained by sonochemical precipitation. The products mainly consist of randomly agglomerated planar structures, like those obtained by traditional precipitation and resembling the structure of regular leaves [14]. To gain more quantitative information about these CuO NLs, size histograms for length (L, Fig. 2(b)), width (W, Fig. 2(c)), and thickness (T, Fig. 2(d)) were constructed. The histograms indicate that CuO NLs obtained by sonochemical precipitation are slightly larger (1080 nm vs. 602 nm), wider (286 nm vs. 219 nm) and thinner (26 nm vs. 15 nm) than those of our previous work, evidencing that the incorporation of the ultrasonic bath can be an important parameter in tuning the size of the NLs. The electrokinetic potential of the CuO NLs was (-21 ± 5) mV at pH = 5.5, which is similar to previously reported values for CuO nanostructures [38,39]. At pH = 7.0 the zeta potential changes to (-30 ± 3) mV. A

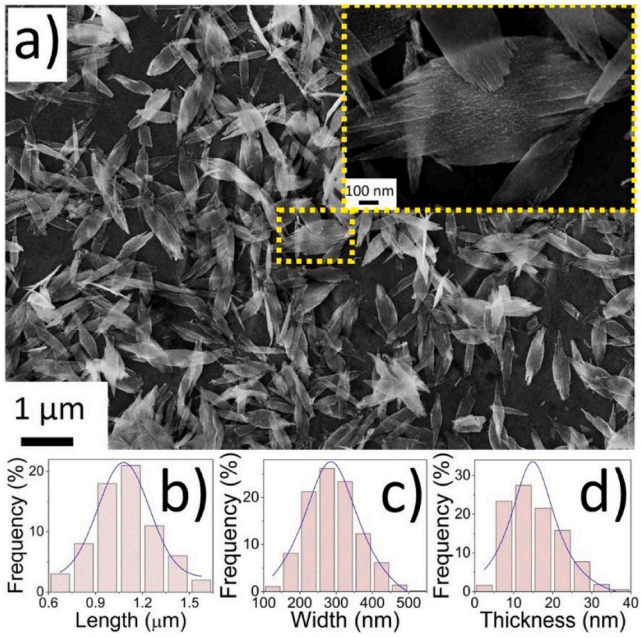

Fig. 2. **(a)** FE-SEM image of CuO NLs fabricated by sonochemical precipitation. The inset shows a magnification of the selected area. Histograms show the NLs **(b)** length, **(c)** width, and **(d)** thickness.

similar value has been reported for other stable NLs dispersions [40]. According to these results, the Fe_3O_4 NPs and the CuO NLs have well-defined and opposite charges at pH = 5.5, so we decided to conduct the coupling reaction under these conditions to boost the electrostatic attraction and facilitate the flocculation process between the two precursors.

3.3. Characterization of Fe_3O_4/CuO NCs

FE-SEM was used to examine the morphology and the elemental composition of the different Fe_3O_4/CuO NCs systems. As revealed in the microscopy images of Fig. 3, the presence of the Fe_3O_4 NPs and the covering degree of the NLs increase in line with the amount of precursor used during synthesis. For instance, the images of sample 67 % (Figs. 3 (a) and 3(b)) show that many of the Fe_3O_4/CuO NCs have the surface entirely covered by the Fe_3O_4 NPs, while the images of sample 33 % (Figs. 3(e) and 3(f)) show that the Fe_3O_4/CuO NCs have a more exposed surface due to the lower amount of Fe_3O_4 NPs. This difference in coverage may affect the efficiency of the catalyst during the recovery cycles, as will be discussed later. The distribution of the Fe_3O_4 NPs on the NLs surface seems to be somewhat inhomogeneous in the three samples. The elemental composition of the nanocomposites was studied by Energy-Dispersive X-ray spectroscopy (EDX). Fig. 4 shows the EDX spectra of the three Fe_3O_4/CuO NCs systems prepared with different ratios of the precursors. The three nanocomposites are composed of only five elements, without any elemental impurities. The presence of copper, iron, and oxygen atoms can be related to CuO NLs and Fe_3O_4 NPs, while carbon and nitrogen elements can be related to the β-alanine contribution. The amount of the two metallic elements observed in the EDX patterns matches the expected composition according to the precursor's ratio employed in the synthesis. The metallic elements proportion (Fe/Cu) calculated from EDX peaks are 67/33, 50/50, and 29/71 for samples 67 %, 50 %, and 33 % respectively.

Fig. 5 shows the X-ray diffractograms of the Fe_3O_4 NPs, the CuO NLs, and the three Fe_3O_4/CuO NCs systems. The diffraction peaks observed in CuO NLs can be indexed to a monoclinic structure (CuO, JCPDS PDF Card no. 80–1916), while the Fe_3O_4 NPs can be indexed to the typical cubic spinel structure assigned to the iron oxide phase magnetite (Fe_3O_4,

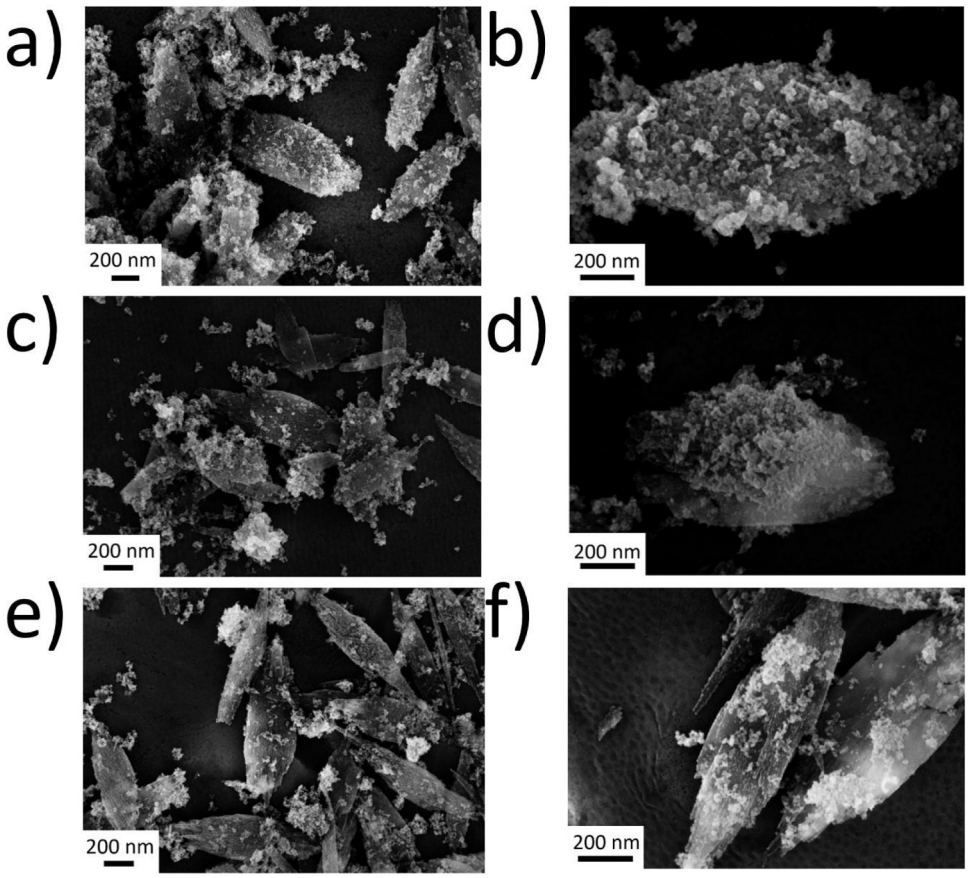

Fig. 3. FE-SEM images of the Fe_3O_4/CuO NCs systems **(a-b)** Sample 67 %; **(c-d)** Sample 50 %; and **(e-f)** Sample 33 %.

JCPDS card No. 19–629) and/or maghemite (δ-Fe_2O_3, JCPDS card No. 39–1346). For the Fe_3O_4/CuO NCs systems, the diffraction peaks of the diffractograms are consistent with the original precursors cupric oxide and iron oxide structures. No strong modifications of the original crystallographic phases nor the appearance of new ones were observed by mixing the nanostructures. The only difference between these systems is the relative intensity of the peaks.

The average crystallite size (D) and the average local root-mean-square strain $\left(\langle \varepsilon_0^2 \rangle^{\frac{1}{2}}\right)$ of CuO NLs and Fe_3O_4 NPs were determined using the single-line method [41]. Results are depicted in Table 1. The D value of CuO NLs agrees with the average thickness of the leaves. Meanwhile, the nanoparticles' crystallite size is closer to the particle size presented before. These results show the polycrystalline nature of CuO NLs and the single-crystalline nature of the Fe_3O_4 NPs. The differences in the $\langle \varepsilon_0^2 \rangle^{\frac{1}{2}}$ values between the two precursors are related to the crystallite size, as smaller D values could increase the lattice strain due to atomic dislocation [42].

The Cohen method was used to obtain additional evidence of the lattice parameters of the samples, considering a monoclinic and a cubic spinel structure for cupric oxide and iron oxide, respectively. Results are depicted in Table 1 and agree with those reported in the literature for CuO bulk material [43]. In the case of iron oxide, the lattice parameter is slightly different from that expected in the bulk material [22]. The presence of strains is more significant in NPs than in NLs. In both cases, the unit cell volume (V) values are smaller than the respective bulk state value. These observations agree with our previous results [14] and with the fact that the lattice parameters are contracted in nanostructured systems [44].

Regarding the colloidal behavior of the nanocomposites, the three systems produced in this work can remain suspended and do not settle to the bottom of their container for at least 1 hour, which is enough time to carry out the optical characterization and the MO degradation experiments.

Kubelka-Munk function F(R) or the remission function was used to obtain the band-gap energy (E_g) after processing and analyzing the diffuse reflectance spectra [45]. Fig. 6(a) shows the UV-Vis diffuse reflectance spectra of the Fe_3O_4 NPs, CuO NLs and the Fe_3O_4/CuO NCs. These measurements provide information about the scattering and absorption coefficients of samples and, hence, their optical properties. Fig. 6(a) shows that the absorption value of all samples decreases as the wavelength increases. This is an expected behavior for semiconductor systems, where the absorption coefficient increases with the photon energy. The curves for CuO NLs and Fe_3O_4 NPs have the lowest and the highest reflectance intensity for any wavelength, respectively. Meanwhile, the spectra of the nanocomposites are in between these measurements, behaving as a combination of these two extreme cases.

From the reflectance spectra it is possible to apply the Kubelka-Munk function F(R):

$$F(R) = \frac{(1-R)^2}{2R} \tag{1}$$

where R is the absolute value of reflectance. In Kubelka-Munk theory, $F(R)$ is equivalent to the absorption coefficient and is related to the band-gap energy according to Tauc's relation:

$$F(R).h\nu = A(h\nu - E_g)^n \tag{2}$$

where A is a constant, $h\nu$ is the photon energy, E_g is the band-gap energy, and n is an index that depends on the nature of electronic transition [46]. The types of electronic transitions are direct allowed ($n = 1/2$), direct

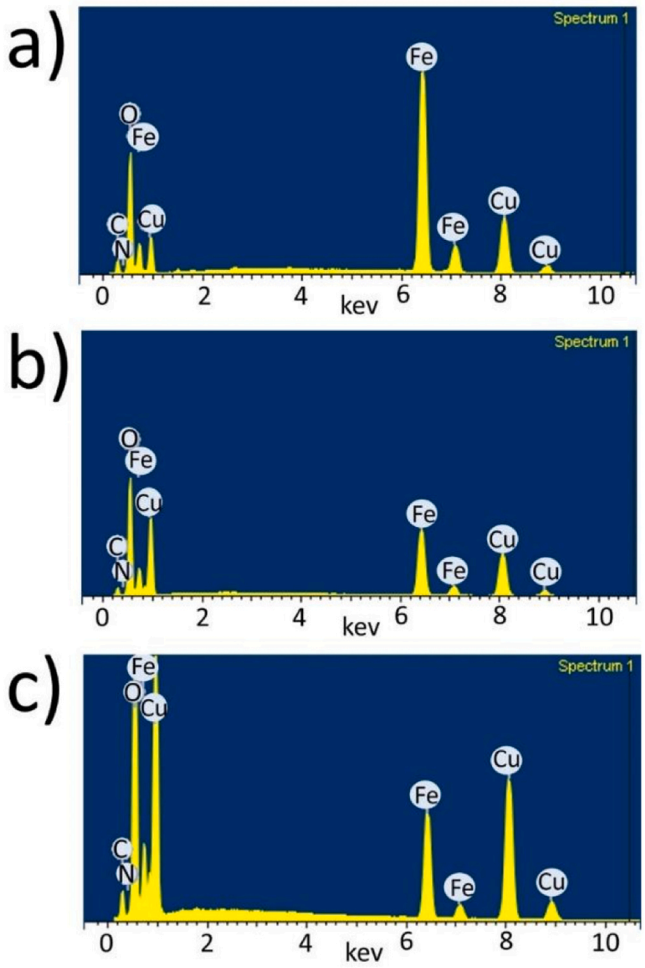

Fig. 4. EDX patterns of the Fe_3O_4/CuO NCs systems **(a)** Sample 67 %; **(b)** Sample 50 %; and **(c)** Sample 33 %.

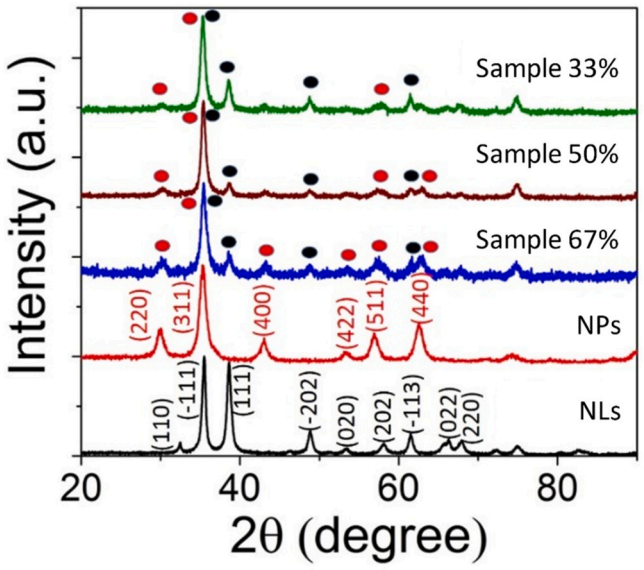

Fig. 5. X-ray diffraction patterns of the primary nanostructures and the Fe_3O_4/CuO NCs systems. The black and red dots correspond with cupric oxide and magnetite diffractions, respectively.

Table 1
Structural parameters from XRD analysis. Average crystallite size (D) and local root-mean-square strain $\left(\langle\varepsilon_0^2\rangle^{\frac{1}{2}}\right)$ from single-line method. Lattice parameters (a, b, c, and β) and volume of the unit cell (V) from Cohen method. V^* corresponds to the unit cell volume of the bulk state.

Sample	*Single-line*		*Cohen Method*					
	D (nm)	$\langle\varepsilon_0^2\rangle^{\frac{1}{2}}$	*a (Å)*	*b (Å)*	*c (Å)*	*β*	*V (Å³)*	*V* (Å³)*
CuO NLs	16	0.003	4.67	3.42	5.12	99.1°	80.7	81.1
Fe_3O_4 NPs	10	0.007	8.36	8.36	8.36	90°	584	592

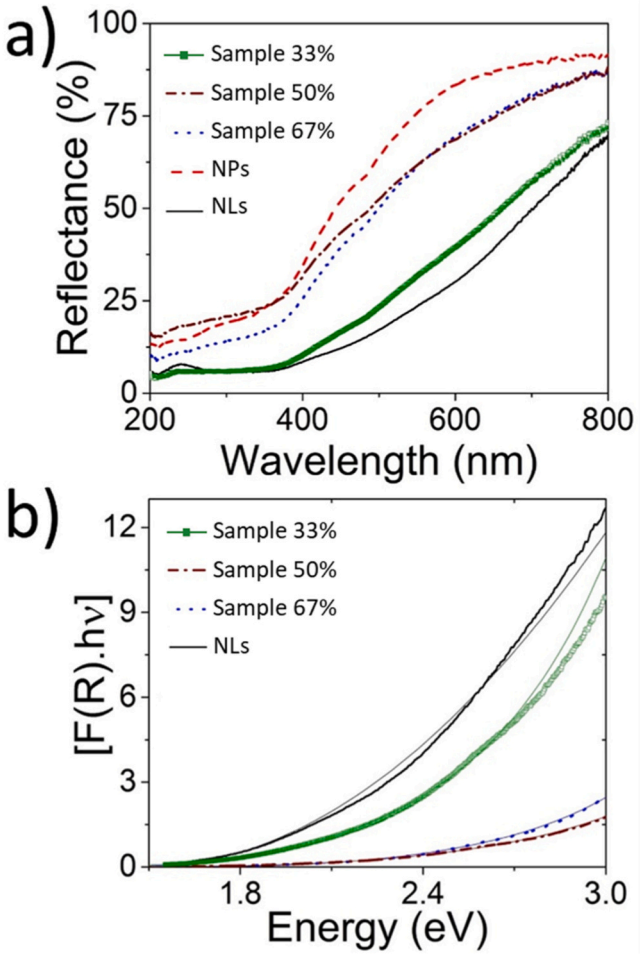

Fig. 6. Optical properties of the Fe_3O_4 NPs, CuO NLs, and Fe_3O_4/CuO NCs **(a)** Reflectance vs. wavelength spectra **(b)** Absorption coefficient, $F(R)$, vs. photon energy, $h\nu$.

forbidden ($n = 3/2$), indirect allowed ($n = 2$) and indirect forbidden ($n = 3$). Eq. (2) has been widely used for determining the E_g of cupric oxide nanostructures [43]. At first glance, due to the two phases that make up the nanocomposites, it expected two band-gaps. However, the results shown in Fig. 6(b) show one value and agree with previous theoretical reports for the band structure theory of Fe_3O_4, which suggest small values (0.2 eV) characteristic for semimetal materials [22,47,48]. Moreover, Milichko et al. [48] reported two interband transitions for Fe_3O_4 NPs between 2.3 and 2.6 eV. These values are closer to those shown in Table 2, so we believe they correspond to this interband transition more than the band-gap energy. For that reason, in our

Table 2
Energy of the direct electronic transitions for Fe_3O_4 NPs obtained by fitting Eq. (2) to the experimental data compared with those reported in the literature.

Transition Energy (eV)	*Size (nm)*	*Reference*
2.7	11	This study
2.2	11	[49]
2.1	10	[50]
2.5–2.6	25	[51]
1.9	10	[52]

opinion, the iron oxide band-gap energy value should not be determined using Eq. (2).

Fig. 6(b) shows $F(R).h\nu$ as a function of the photon energy for CuO NLs and Fe_3O_4/CuO NCs. Every curve of Fig. 6(b) was fitted using Eq. (2) and $n = 2$ because the indirect allowed electronic transition gave the best results ($r^2 > 0.999$). Table 3 shows the band-gap energies obtained from the fitting. For CuO NLs, the obtained E_g value and the type of electronic transition considered are like those reported in our previous work [14]. The absorption onset of nanocomposites showed a blue shift, toward lower light wavelengths, giving rise to an increase in the band-gap energy up to 1.78 eV. Previous reports describing the optical properties of Fe_3O_4@CuO core-shell nanostructures have reported a band-gap energy of 1.87 eV, which is similar to the value measured for sample 67 % [30]. The increase of the band-gap energy of the Fe_3O_4/-CuO NCs with an increase in the Fe_3O_4 NPs content suggests that it is possible to tune this property by this mechanism. The coupling between the band structure of the NLs and NPs could be responsible for the modifications of the band-gap energy. Similar behaviors have been reported for graphene decorated with metal nanoparticles [53].

3.4. Sonocatalytic activity of Fe_3O_4/CuO NCs

Due to the specific properties of the primary NPs and NLs, and the synergistic structure observed in the nanocomposites, the Fe_3O_4/CuO NCs prepared in this work may have potential as effective and reusable catalysts. To prove this point, nanocomposites were used as catalysts for the oxidative degradation of methyl orange dye aqueous solution. The degradation experiments were conducted in the presence of selected samples acting as a catalyst and in dark conditions to avoid photocatalysis. The reaction was assisted by an oxidizing agent (hydrogen peroxide, H_2O_2) and ultrasound. Fig. 7(a) shows the UV-Vis spectra of the different mixtures after 1 h of reaction and 20 min of magnetic separation for each one of the catalysts. The degradation percentage was calculated according to the following expression:

$$\%Degradation = \frac{C_0 - C_i}{C_0} \times 100 \quad (3)$$

where C_0 is the initial concentration of MO and C_i is the final concentration of MO after the experiment. The concentration was determined from the absorbance of the solution at 465 nm. When the reaction proceeds with the Fe_3O_4 NPs as the catalyst the degradation of the dye is about 49 %. The incomplete degradation of MO when using Fe_3O_4 NPs alone suggests that this nanomaterial is not an efficient catalyst for this reaction under the experimental conditions of this work. When the same reaction mixture was tested in the presence of the three Fe_3O_4/CuO NCs the absorption band of MO nearly disappears. These results prove a full degradation of the organic dye and suggest that the surface of the NLs is exposed enough to catalyze the reaction independently of the NPs concentration in the nanocomposite. A sequence of photographs of the reaction showing the degradation and isolation process is presented in Fig. 7(b). In our previous work [14], we demonstrated that the CuO NLs are highly efficient for the MO degradation at the same experimental conditions used in this work, and we prove that this catalytic activity can be preserved in the nanocomposites. No degradation was observed when the experiments were performed with the NCs and the dye but without H_2O_2 or sonication.

Table 3
Indirectly allowed band-gap energies (E_g) obtained for CuO NLs and Fe_3O_4/CuO NCs from Eq. (2) and Fig. 6(b).

Sample	*E_g(eV)*
CuO NLs	1.48
NCs 33 %	1.52
NCs 50 %	1.67
NCs 67 %	1.78

The CuO dosage relative to MO in each one of the experiments was 4.2, 6.3, and 8.3 wt for samples 67 %, 50 % and 33 %, respectively. The NLs concentrations are in the same order as those reported in our previous work [14] and, to the best of our knowledge, correspond to one of the lowest catalyst dosages for MO degradation reported in the literature. Therefore, the three Fe_3O_4/CuO NCs of this work could be considered effective catalysts for MO degradation. Besides this activity, the main advantage of the proposed catalyst is their magnetic recovery potential, which is an easier and lower cost technique than the traditional centrifugation or filtration method. Also, we cannot rule out that the presence of the Fe_3O_4 phase could lead to the occurrence of charge transfer events, which could increase the activity in the CuO surface and enhance the catalytic performance of the nanocomposites. It could be possible that the close contact between NLs and NPs at the interface can make electrons diffuse from the iron oxide Fermi level to the conduction band of cupric oxide. This process leads to a downward band bending of the metal oxide, which causes charge accumulation at the interface that can promote the formation of reactive oxygen species (ROS) when the nanocomposites trigger the reaction of H_2O_2 molecules with the assistance of ultrasonication. The ROS (such as superoxide, O_2^-, and hydroxyl radicals, ·OH) produced in this process can then participate in the degradation reactions of the organic dyes by breaking these molecules into smaller units, enhancing the catalytic activity of the nanocomposites.

The reusability and stability of the three Fe_3O_4/CuO NCs were explored after they showed excellent catalytic activity for MO degradation. The dye degradation experiments were performed with the same initial conditions after recycling the catalyst by collecting the nanocomposite at the bottom of a flask with a magnet and washing it three times. Fig. 7(c) shows that the degradation efficiency somewhat decreases with the cycle number, with the sample 67 % showing the lowest performance on the third cycle. In this sample the large extent of NPs may favor the magnetic recovery of the nanocomposites but, at the same time, it may cause a lower efficiency of degradation, like the one exhibited by Fe_3O_4 NPs alone. Also, the SEM images of the NCs revealed that the proportion of Fe_3O_4 NPs to CuO NLs used in the synthesis of this system results in the lowest exposed CuO surface among the three samples, possibly leading to faster saturation of the surface due to the smaller total catalytic area. On the other hand, the samples 33 % and 50 % show the best reusability results after three cycles, indicating that optimal synergistic effect is achieved with a NPs / NLs ratio between these values. The efficiency in the third cycle is approximately 60 % and is higher than the one obtained when the CuO NLs are recovered by centrifugation [14]. These results also prove that magnetic recovery could be more efficient than the centrifugation process.

4. Conclusions

Polycrystalline CuO NLs and single-crystalline Fe_3O_4 NPs were successfully synthesized by simple and low-cost precipitation techniques. By mixing an aqueous suspension of both nanostructures at 65 °C, we were able to produce three different nanocomposites of Fe_3O_4/CuO NCs. The easy association of the primary NLs and NPs within our reaction medium is driven by attractive electrostatic forces arising from the opposite charges present in these nanostructures. The formation of these

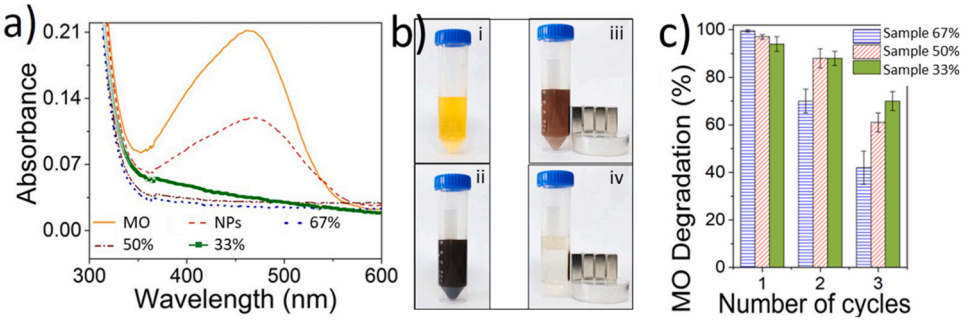

Fig. 7. **(a)** UV-Vis absorption spectra of the MO solution and the reaction mixtures after the degradation process for 1 h with the different catalysts. **(b)** Photographs depicting the degradation process of MO by the Fe_3O_4/CuO NCs. (i) MO solution, (ii) mixture of the catalyst and MO before degradation, (iii) mixture after degradation and 1 min of magnetic separation, and (iv) mixture after degradation and 5 min of magnetic separation. **(c)** % of degradation of MO for successive reaction and magnetic recovery cycles of the different catalysts.

nanocomposites was confirmed through detailed SEM imaging, revealing structures consisting of CuO NLs approximately 1.2 μm in length, covered with Fe_3O_4 NPs of around 11 nm in diameter. X-ray diffraction patterns of the Fe_3O_4/CuO NCs indicate no significant structural alterations or changes in crystallographic phases when compared to the primary nanostructures. Also, the Fe_3O_4/CuO NCs presented an increase in the band-gap energy with the concentration of Fe_3O_4 NPs. By studying the catalytic oxidative degradation of methyl orange, we showed that the Fe_3O_4/CuO NCs can be employed as highly efficient and easily recyclable catalysts. The catalytic power of these nanocomposites can be attributed to the presence of CuO NLs, and the magnetic characteristics introduced by the Fe_3O_4 NPs offer the potential for magnetically assisted recovery. Although these initial results are encouraging and demonstrates the potential of Fe_3O_4/CuO NCs as effective catalysts for water remediation, additional studies are needed to go beyond the limitations that this work presents. Among others, these future works must include the analysis of the catalytic performance in a broader range of contaminants, and a system scalability analysis. Addressing these aspects can help us realize the full potential of our Fe_3O_4/CuO NCs as a truly compelling solution for water treatment applications.

CRediT authorship contribution statement

César Leandro Londoño-Calderón: Conceptualization, Methodology, Investigation, Data Curation, Writing – original draft. **Pablo Tancredi:** Methodology, Investigation, Writing – review and editing. **Sandra Menchaca-Nal:** Investigation, Formal analysis, Writing – review and editing. **Nora J. Francois:** Funding acquisition, Resources, Writing – review and editing. **Laura G. Pampillo:** Conceptualization, Project administration, Writing – review and editing.

Declaration of Competing Interest

The authors declare that they have no known competing financial interests or personal relationships that could have appeared to influence the work reported in this paper.

Acknowledgments

This work was supported by Agencia Nacional de Promoción Científica y Tecnológica (Préstamo BID through projects PICT 2014–1955 and 2016–0843), CONICET (PUE 22920160100034CO and PUE 22920170100073CO), Universidad de Buenos Aires (UBACyT 20020190200304BA) and Ministerio de Ciencia Tecnología e Innovación - Colombia (Grant No 903–2021 - "BIOFÁBRICAS: una oportunidad de desarrollo bioeconómico para Caldas a través de la biotecnología", código 86957, que integra el desarrollo de tres proyectos: (i) 3BIO: Analítica de datos de Biodiversidad, Bioprospección y Biotecnología como estrategia para el desarrollo de la bioeconomía en Colombia, código 87053; (ii) Creación de una estrategia de gobernanza del modelo bioeconómico de las biofábricas en el departamento de Caldas, código 87054; (iii) Desarrollo de productos de base biotecnológica para el encadenamiento productivo de las biofábricas, código 87055). C.L.L.C and S.M.N thank CONICET for their postdoctoral scholarships. C.L.L.C acknowledges "Unidad de Investigación" from Universidad Autónoma de Manizales (Colombia). The authors want to thank Dr. Pablo Froimowicz from the Design and Chemistry of Macromolecules Group, Institute of Technology in Polymers and Nanotechnology - ITPN, UBA-CONICET, for all the collaboration.

References

[1] K. Valizadeh, A. Bateni, N. Sojoodi, M.R. Ataabadi, A.H. Behroozi, A. Maleki, Z. You, Magnetized inulin by Fe3O4 as a bio-nano adsorbent for treating water contaminated with methyl orange and crystal violet dyes, Sci. Rep. 12 (2022) 22034, https://doi.org/10.1038/s41598-022-26652-7.

[2] M. Malhotra, A. Sudhaik, Sonu, P. Raizada, T. Ahamad, V.-H. Nguyen, Q. Van Le, R. Selvasembian, A.K. Mishra, P. Singh, An overview on cellulose-supported photocatalytic materials for the efficient removal of toxic dyes, Ind. Crops Prod. 202 (2023) 117000, https://doi.org/10.1016/j.indcrop.2023.117000.

[3] B. Lellis, C.Z. Fávaro-Polonio, J.A. Pamphile, J.C. Polonio, Effects of textile dyes on health and the environment and bioremediation potential of living organisms, Biotechnol. Res. Innov. 3 (2019) 275–290, https://doi.org/10.1016/j.biori.2019.09.001.

[4] M. Kloster, A.A. de Almeida, D. Muraca, N.E. Marcovich, M.A. Mosiewicki, Chitosan-based magnetic particles as adsorbents for anionic contaminants, Eng. Sci. (2023), https://doi.org/10.30919/es8d851.

[5] A. Aljuaid, M. Almehmadi, A.A. Alsaiari, M. Allahyani, O. Abdulaziz, A. Alsharif, J. A. Alsaiari, M. Saih, R.T. Alotaibi, I. Khan, g-C3N4 based photocatalyst for the efficient photodegradation of toxic methyl orange dye: recent modifications and future perspectives, Molecules 28 (2023), https://doi.org/10.3390/molecules28073199.

[6] C.S.D. Rodrigues, L.M. Madeira, R.A.R. Boaventura, Synthetic textile dyeing wastewater treatment by integration of advanced oxidation and biological processes – Performance analysis with costs reduction, J. Environ. Chem. Eng. 2 (2014) 1027–1039, https://doi.org/10.1016/j.jece.2014.03.019.

[7] P. Moradihamedani, Recent advances in dye removal from wastewater by membrane technology: a review, Polym. Bull. 79 (2022) 2603–2631, https://doi.org/10.1007/s00289-021-03603-2.

[8] M.M. Al-Ansari, Z. Li, A. Masood, J. Rajaselvam, Decolourization of azo dye using a batch bioreactor by an indigenous bacterium Enterobacter aerogenes ES014 from the waste water dye effluent and toxicity analysis, Environ. Res 205 (2022) 112189, https://doi.org/10.1016/j.envres.2021.112189.

[9] F. Ghanbari, M. Moradi, A comparative study of electrocoagulation, electrochemical Fenton, electro-Fenton and peroxi-coagulation for decolorization of real textile wastewater: Electrical energy consumption and biodegradability improvement, J. Environ. Chem. Eng. 3 (2015) 499–506, https://doi.org/10.1016/j.jece.2014.12.018.

[10] B. Othmani, J.A.F. Gamelas, M.G. Rasteiro, M. Khadhraoui, Characterization of two cactus formulation-based flocculants and investigation on their flocculating ability for cationic and anionic dyes removal, Polymers 12 (2020) 1964, https://doi.org/10.3390/polym12091964.

[11] D.L.T. Nguyen, Q.A. Binh, X.C. Nguyen, T.T. Huyen Nguyen, Q.N. Vo, T.D. Nguyen, T.C. Phuong Tran, T.A. Hang Nguyen, S.Y. Kim, T.P. Nguyen, J. Bae, I.T. Kim, Q. Van Le, Metal salt-modified biochars derived from agro-waste for effective

congo red dye removal, Environ. Res. 200 (2021) 111492, https://doi.org/10.1016/j.envres.2021.111492.
[12] R. Dewil, D. Mantzavinos, I. Poulios, M.A. Rodrigo, New perspectives for advanced oxidation processes, J. Environ. Manag. 195 (2017) 93–99, https://doi.org/10.1016/j.jenvman.2017.04.010.
[13] P. Verma, S.K. Samanta, Microwave-enhanced advanced oxidation processes for the degradation of dyes in water, Environ. Chem. Lett. 16 (2018) 969–1007, https://doi.org/10.1007/s10311-018-0739-2.
[14] C.L. Londoño-Calderón, S. Menchaca-Nal, N.J. François, L.G. Pampillo, P. Froimowicz, Cupric oxide nanoleaves for the oxidative degradation of methyl orange without heating or light, ACS Appl. Nano Mater. 3 (2020) 2987–2996, https://doi.org/10.1021/acsanm.0c00283.
[15] R. Oder, High gradient magnetic separation theory and applications, IEEE Trans. Magn. 12 (1976) 428–435, https://doi.org/10.1109/TMAG.1976.1059076.
[16] M. Saberian, A. Nezamzadeh-Ejhieh, Synergistic photocatalytic degraded tetracycline upon supported CuO clinoptilolite nanoparticles, Solid State Sci. 147 (2024) 107381, https://doi.org/10.1016/j.solidstatesciences.2023.107381.
[17] R.B. Nasir Baig, M.N. Nadagouda, R.S. Varma, Magnetically retrievable catalysts for asymmetric synthesis, Coord. Chem. Rev. 287 (2015) 137–156, https://doi.org/10.1016/j.ccr.2014.12.017.
[18] L.M. Rossi, N.J.S. Costa, F.P. Silva, R. Wojcieszak, Magnetic nanomaterials in catalysis: advanced catalysts for magnetic separation and beyond, Green. Chem. 16 (2014) 2906–2933, https://doi.org/10.1039/C4GC00164H.
[19] Á. Molnár, A. Papp, Catalyst recycling—A survey of recent progress and current status, Coord. Chem. Rev. 349 (2017) 1–65, https://doi.org/10.1016/j.ccr.2017.08.011.
[20] A.K. Vishwakarma, B.Sen Yadav, A.K. Singh, S. Kumar, N. Kumar, Magnetically recyclable ZnO coated Fe3O4 nanocomposite for MO dye degradation under UV-light irradiation, Solid State Sci. 145 (2023) 107312, https://doi.org/10.1016/j.solidstatesciences.2023.107312.
[21] R. Hudson, Y. Feng, R.S. Varma, A. Moores, Bare magnetic nanoparticles: sustainable synthesis and applications in catalytic organic transformations, Green. Chem. 16 (2014) 4493–4505, https://doi.org/10.1039/C4GC00418C.
[22] R.M. Cornell, U. Schwertmann, The Iron Oxides, Wiley, 2003, https://doi.org/10.1002/3527602097.
[23] D. Bai, P. Yan, Magnetic nanoscaled Fe3O4 as an efficient and reusable heterogeneous catalyst for degradation of methyl orange in microwave-enhanced fenton-like system, Appl. Mech. Mater. 448 (2013) 830–833, https://doi.org/10.4028/www.scientific.net/AMM.448-453.830.
[24] H. Jiang, Y. Sun, J. Feng, J. Wang, Heterogeneous electro-Fenton oxidation of azo dye methyl orange catalyzed by magnetic Fe3O4 nanoparticles, Water Sci. Technol. 74 (2016) 1116–1126, https://doi.org/10.2166/wst.2016.300.
[25] Y. Lei, C.-S. Chen, Y.-J. Tu, Y.-H. Huang, H. Zhang, Heterogeneous Degradation of Organic Pollutants by Persulfate Activated by CuO-Fe3O4: mechanism, stability, and effects of pH and bicarbonate ions, Environ. Sci. Technol. 49 (2015) 6838–6845, https://doi.org/10.1021/acs.est.5b00623.
[26] A. Taufik, I. Kalim, R. Saleh, Preparation, characterization and photocatalytic activity of multifunctional Fe3O4/ZnO/CuO hybrid nanoparticles, Mater. Sci. Forum 827 (2015) 37–42, https://doi.org/10.4028/www.scientific.net/MSF.827.37.
[27] A. Taufik, R. Saleh, Synthesis of iron(II,III) oxide/zinc oxide/copper(II) oxide (Fe3O4/ZnO/CuO) nanocomposites and their photosonocatalytic property for organic dye removal, J. Colloid Interface Sci. 491 (2017) 27–36, https://doi.org/10.1016/j.jcis.2016.12.018.
[28] A.H. Kianfar, M.A. Arayesh, Synthesis, characterization and investigation of photocatalytic and catalytic applications of Fe3O4/TiO2/CuO nanoparticles for degradation of MB and reduction of nitrophenols, J. Environ. Chem. Eng. 8 (2020) 103640, https://doi.org/10.1016/j.jece.2019.103640.
[29] A.Q. Alorabi, M. Shamshi Hassan, M. Azizi, Fe3O4-CuO-activated carbon composite as an efficient adsorbent for bromophenol blue dye removal from aqueous solutions, Arab J. Chem. 13 (2020) 8080–8091, https://doi.org/10.1016/j.arabjc.2020.09.039.
[30] J. Ding, L. Liu, J. Xue, Z. Zhou, G. He, H. Chen, Low-temperature preparation of magnetically separable Fe3O4@CuO-RGO core-shell heterojunctions for high-performance removal of organic dye under visible light, J. Alloy. Compd. 688 (2016) 649–656, https://doi.org/10.1016/j.jallcom.2016.07.001.
[31] P. Tancredi, L.S. Veiga, O. Garate, G. Ybarra, Magnetophoretic mobility of iron oxide nanoparticles stabilized by small carboxylate ligands, Colloids Surf. A Physicochem Eng. Asp. 579 (2019) 123664, https://doi.org/10.1016/j.colsurfa.2019.123664.
[32] C.L.L. Calderón, S.M. Nal, D.C.P. Saavedra, J. Silveyra, L.M. Socolovsky, L. G. Pampillo, R.M. García, Fabricación de alúmina anódica porosa de bajo costo: Un estudio comparativo de la morfología producida por uno y dos pasos de anodizad, Rev. Mater. 21 (2016) 677–690, https://doi.org/10.1590/S1517-707620160003.0065.
[33] A. Doğan, F. Köseoğlu, E. Kılıç, The stability constants of copper(II) complexes with some α-amino acids in dioxan–water mixtures, Anal. Biochem 295 (2001) 237–239, https://doi.org/10.1006/abio.2001.5205.
[34] A. Ditsch, P.E. Laibinis, D.I.C. Wang, T.A. Hatton, Controlled clustering and enhanced stability of polymer-coated magnetic nanoparticles, Langmuir 21 (2005) 6006–6018, https://doi.org/10.1021/la047057+.
[35] D. Jara, L.S. Veiga, O. Garate, G. Ybarra, P. Tancredi, Mass-production of water-based ferrofluids capable of developing spike-like structures, J. Magn. Magn. Mater. 572 (2023) 170622, https://doi.org/10.1016/j.jmmm.2023.170622.
[36] S. Bhattacharjee, DLS and zeta potential – What they are and what they are not? J. Control Release 235 (2016) 337–351, https://doi.org/10.1016/j.jconrel.2016.06.017.
[37] Z.-X. Sun, F.-W. Su, W. Forsling, P.-O. Samskog, Surface Characteristics of Magnetite in Aqueous Suspension, J. Colloid Interface Sci. 197 (1998) 151–159, https://doi.org/10.1006/jcis.1997.5239.
[38] I. Rasoulpour, S. Jafarirad, Synthesis of biocapped CuO nanoparticles: an investigation on biorganic-Cu2+ interactions, in vitro antioxidant and antimicrobial aspects, Inorg. Nano-Met. Chem. 47 (2017) 1599–1604, https://doi.org/10.1080/24701556.2017.1357615.
[39] M. Volland, M. Hampel, A. Katsumiti, M.P. Yeste, J.M. Gatica, M. Cajaraville, J. Blasco, Synthesis methods influence characteristics, behaviour and toxicity of bare CuO NPs compared to bulk CuO and ionic Cu after in vitro exposure of Ruditapes philippinarum hemocytes, Aquat. Toxicol. 199 (2018) 285–295, https://doi.org/10.1016/j.aquatox.2018.04.007.
[40] M.I. Nabila, K. Kannabiran, Biosynthesis, characterization and antibacterial activity of copper oxide nanoparticles (CuO NPs) from actinomycetes, Biocatal. Agric. Biotechnol. 15 (2018) 56–62, https://doi.org/10.1016/j.bcab.2018.05.011.
[41] E.J. Mittemeijer, U. Welzel, The "state of the art" of the diffraction analysis of crystallite size and lattice strain, Z. Krist. Cryst. Mater. 223 (2008) 552–560, https://doi.org/10.1524/zkri.2008.1213.
[42] H. Siddiqui, M.R. Parra, F.Z. Haque, Optimization of process parameters and its effect on structure and morphology of CuO nanoparticle synthesized via the sol−gel technique, J. Solgel Sci. Technol. 87 (2018) 125–135, https://doi.org/10.1007/s10971-018-4663-5.
[43] Q. Zhang, K. Zhang, D. Xu, G. Yang, H. Huang, F. Nie, C. Liu, S. Yang, CuO nanostructures: Synthesis, characterization, growth mechanisms, fundamental properties, and applications, Prog. Mater. Sci. 60 (2014) 208–337, https://doi.org/10.1016/j.pmatsci.2013.09.003.
[44] C.Q. Sun, Size dependence of nanostructures: impact of bond order deficiency, Prog. Solid State Chem. 35 (2007) 1–159, https://doi.org/10.1016/j.progsolidstchem.2006.03.001.
[45] E.L. Simmons, Diffuse reflectance spectroscopy: a comparison of the theories, Appl. Opt. 14 (1975) 1380, https://doi.org/10.1364/AO.14.001380.
[46] W.J. Jeyarani, T. Tenkyong, N. Bachan, D.A. Kumar, J.M. Shyla, An investigation on the tuning effect of glucose-capping on the size and bandgap of CuO nanoparticles, Adv. Powder Technol. 27 (2016) 338–346, https://doi.org/10.1016/j.apt.2016.01.006.
[47] H. Liu, C. Di Valentin, Band gap in magnetite above verwey temperature induced by symmetry breaking, J. Phys. Chem. C. 121 (2017) 25736–25742, https://doi.org/10.1021/acs.jpcc.7b09387.
[48] V.A. Milichko, A.I. Nechaev, V.A. Valtsifer, V.N. Strelnikov, Y.N. Kulchin, V. P. Dzyuba, Photo-induced electric polarizability of Fe3O4 nanoparticles in weak optical fields, Nanoscale Res. Lett. 8 (2013) 317, https://doi.org/10.1186/1556-276X-8-317.
[49] Y. Bagbi, A. Sarswat, D. Mohan, A. Pandey, P.R. Solanki, Lead (Pb2+) adsorption by monodispersed magnetite nanoparticles: surface analysis and effects of solution chemistry, J. Environ. Chem. Eng. 4 (2016) 4237–4247, https://doi.org/10.1016/j.jece.2016.09.026.
[50] Y. Bagbi, A. Sarswat, D. Mohan, A. Pandey, P.R. Solanki, Lead and chromium adsorption from water using l-cysteine functionalized magnetite (Fe3O4) nanoparticles, Sci. Rep. 7 (2017) 7672, https://doi.org/10.1038/s41598-017-03380-x.
[51] A. Muzammil, D. Taufiq, Y.A. Yuliantika, Hariyanto, A. Sunaryono, S. Hidayat, N. Bahtiar, N. Mufti, Hidayat, effect of template on structural and band gap behaviors of magnetite nanoparticles, J. Phys. Conf. Ser. 1093 (2018) 012020, https://doi.org/10.1088/1742-6596/1093/1/012020.
[52] H. El Ghandoor, H.M. Zidan, M.M.H. Khalil, M.I.M. Ismail, Synthesis and some physical properties of magnetite (Fe3O4) nanoparticles, Int J. Electrochem Sci. 7 (2012) 5734–5745, https://doi.org/10.1016/S1452-3981(23)19655-6.
[53] P. Bazylewski, A. Akbari-Sharbaf, S. Ezugwu, T. Ouyang, J. Park, G. Fanchini, Graphene thin films and graphene decorated with metal nanoparticles. Crystalline and Non-Crystalline Solids, InTech, 2016, https://doi.org/10.5772/63279.